Journal of Rare Earths 35 (2017) 1102–1114

Contents lists available at ScienceDirect

Journal of Rare Earths

journal homepage: http://www.journals.elsevier.com/journal-of-rare-earths

Experimental charge density distribution and its correlation to structural and optical properties of Sm^{3+} doped Nd_2O_3 nanophosphors

Morris Marieli Antoinette [a], S. Israel [a, *], G. Sathya [b], Arlin Jose Amali [c], John L. Berchmans [b], K. Sujatha [a], C. Anzline [a], R. Niranjana Devi [a]

[a] Post Graduate and Research Department of Physics, The American College, Madurai 625 002, Tamilnadu, India
[b] Electro-Pyrometallurgy Division, CSIR-Central Electrochemical Research Institute, Karaikudi 630 003, Tamilnadu, India
[c] School of Chemistry, Madurai Kamaraj University, Madurai, 625 021, Tamilnadu, India

ARTICLE INFO

Article history:
Received 4 January 2017
Received in revised form
13 April 2017
Accepted 14 April 2017
Available online 18 August 2017

Keywords:
Modified Pechini method
Photoluminescence
MEM/Rietveld
Charge density

ABSTRACT

Pure and Sm^{3+} doped Nd_2O_3 nanophosphors were synthesized using modified Pechini method. The phase formation with symmetry of the sample is confirmed by the Rietveld refinement of the powder X-ray diffraction (PXRD) data. The surface morphology and the crystallite size were examined using scanning electron microscopy (SEM) and transmission electron microscopy (TEM) and the results confirmed that the synthesized particles are in nanosize. The energy-dispersive X-ray (EDX) analysis was done to confirm the purity of the sample. The optical properties of the sample were studied using ultraviolet–visible range (UV–Vis) spectroscopic analysis and photoluminescence studies. The calculated band gap of the synthesized Nd_2O_3 was found to be higher than that of bulk Nd_2O_3. The photoluminescence (PL) of the prepared samples reveals that doping with Sm^{3+} ion has influenced the optical properties. Quantitative investigation on charge density distribution was done by analysing the 3-dimensional and 2-dimensional charge density maps drawn along the bonding directions. The maximum entropy method (MEM)/Rietveld analysis was used for the first time to analyse the charge density in the chosen system. Charge density arrangement in the unit cell is correlated to the analysed photoluminescent (PL) properties. The spectral behaviour of the samples has been explained through charge ordering which are verified using experimental data obtained. The studies on these materials have shown that these nanophosphors will provide promising application for near-ultraviolet light-emitting diodes (n-UV-LEDs).

1. Introduction

The preparation of nanostructured materials has tremendously attracted major scientific interest because nanomaterials show distinctive or improved properties due to their nanoscale dimensions.[1] Synthesizing new materials in the nanoscale is interesting as they often show unique optical, magnetic, electronic and structural properties, which are different from their respective bulk.[2–5] Many nanomaterials consist of well-characterized components possessing photoluminescent properties that can only be accessed at the nanoscale.

Among the rare earth compounds, the rare earth oxides are most stable and have distinctive interesting properties owing to their unique electronic configurations. Due to the particular electronic, optic, magnetic, catalytic and chemical properties, the rare earth oxides with one dimensional structure such as La_2O_3, Sm_2O_3, Gd_2O_3, and Nd_2O_3 have been widely used in many functional devices.[6,7] Moreover, great attention has been drawn in synthesizing oxide phosphors using trivalent rare earth ion dopants. Eu^{3+} doped $LaPO_4$, synthesized using hydrothermal method, showed excellent luminescent properties.[8] Eu^{3+} doped $SrGd_2O_4$ red phosphors, having potential applications in display devices and solid-state lighting when coupled with UV chips, were prepared by homogeneous precipitation followed by combustion process.[9] SrO:Bi^{3+}, Eu^{3+}, a red-blue dichromic phosphor, was synthesized as a luminescent indicator for measuring temperature. Er^{3+} doped Y_2O_3

* Corresponding author.
E-mail address: israel.samuel@gmail.com (S. Israel).

http://dx.doi.org/10.1016/j.jre.2017.04.006
1002-0721/

nanocrystals showed enhanced upconversion emission and can be used better for high-temperature applications, like optical thermometry based on fluorescence intensity ratio technology. A novel Er^{3+}-doped SrO phosphor was synthesized by interlayer solid-state reaction (ISSR) method to fabricate a short-wavelength infrared (SWIR) light-emitting device.[10–12] In the ongoing pursuit of new and useful photoluminescent materials, nanophysics have become a popular strategy for discovery and innovation.

Recently, appreciable efforts have been employed in preparing new phosphors for solid-state lighting with high effectiveness and excellent chemical stability. Also, presently research is focused on discovering novel phosphors which can be excited by UV sources. In developing such a good luminescent material, it is interesting to note that trivalent lanthanide (Ln^{3+}) ions play a very important role with their incompletely filled 4f shell which on absorbing the excitation energy goes to the excited state and later returns to the ground state, resulting in emitting state in the regions ranging from UV to IR. The change in the electrical and optical characteristics of nanoparticles, caused by quantum effects, in turn increases the band gap.[13,14] Widespread research has led to a library of nanoparticles (NP) synthesis techniques while rare earth oxides have been synthesized by various methods including microwave-assisted, solvothermal, solgel, hydrothermal, solution combustion, molten salt method, co-precipitation etc.[11,15–20]

Nd_2O_3 has fascinated many researchers due to its extensive range of applications. It is a semiconductor with wide band gap among rare earth sesquioxides.[21] Among rare-earth ions, the Nd^{3+} ion is recognized as one of the most effective rare-earth ion for solid state lasers in various materials. Neodymium ions could also be promising candidates for upconversion fluorescence and lasers.[22–24] Nowadays Nd_2O_3 has attracted growing interest and opened many new possibilities for various applications. It is one of the most captivating oxides industrially as it has been widely used in ceramic capacitors, ultraviolet absorbent, colour television tubes, colouring glass, catalyst and carbon-arc-light electrodes.[25]

Doping with rare earth (RE) ions that are well known to emit from the UV to the NIR regions increases the rare earth luminescence. RE-doped nanocrystals show advanced chemical and optical properties, including high resistance to photobleaching, sharp emissions and long fluorescence lifetimes. Thus by doping with RE ions in nanomaterials, a novel material having enhanced advantages of luminescent and magnetic properties could be attainable. Samarium oxide (Sm_2O_3) is an important rare earth oxide and has been studied widely because it has variable valence properties. Samarium oxide nanoparticles are thermally stable, chemically stable and suitable for optics, glass, ceramic, catalytic applications, etc.[26,27] Sm^{3+} doping in CeO_2 showed improved structural features and enhanced the reduction behaviour of CeO_2, leading to enhanced autocatalytic activity.[28] The effect of Sm^{3+} doping in the alkali-barium-bismuth-tellurite (LKBBT) glass has enhanced the luminescence parameters.[29] The studies on the temperature-dependent photoluminescence of Sm^{3+}- and Dy^{3+}-doped Gd_2O_3 phosphors proved that these have good potential for the development of thermographic phosphors.[30] The influence of Sm^{3+} doping in $Ba_2CaZn_2Si_6O_{17}$, a novel orange-red emitting phosphor, for near-ultraviolet (n-UV) based white light diodes applications was studied by Annadurai et al.[31] These studies proved that doping with Sm^{3+} has influenced the structural properties of the material and thus charge density distribution, thus enhancing the luminescent properties of the system. Since there is no previous report on the effect of doping of Sm^{3+} in Nd_2O_3, we have chosen Sm^{3+} as a dopant expecting enhanced luminescence because Sm^{3+} has efficient luminescence in the visible region.

In this work, we report on synthesized pure and Sm^{3+} doped Nd_2O_3 using the modified Pechini method, an inexpensive route with less instrumentation, operated at ambient temperature. Using this method, it is possible to achieve an excellent chemical homogeneity due to the molecular mixing of constituents. The advantage of this method over other high temperature methods is that reaction rate is high and has a low temperature of crystallization.[32] It follows the sol-gel inorganic route and uses organic acids for chelate metal ions in solution. We have prepared Nd_2O_3 nanoparticles using this method. Also, to the best of our knowledge, there is no previous literature on the synthesis of Sm^{3+} doped Nd_2O_3 nanocrystalline powders using modified Pechini method.

2. Experimental

Nd_2O_3 and Sm^{3+} doped Nd_2O_3 nanocrystalline powders were prepared using the modified Pechini method. The schematic diagram of the preparation of the samples is depicted in Fig. 1. Nd_2O_3 was dissolved in hot nitric acid to form the nitrate salt. Ethylenediaminetetraacetic acid (EDTA) as the complexation agent and ethylene glycol (EG) as the polymerization agent were used. The nitrate salts was dissolved in an aqueous solution with a molar ratio of EDTA to metal cations [EDTA]/[METAL] = 1 to ensure the metal-EDTA complexation. Further, EG was added to the mixture in a molar ratio of [EDTA]/[EG] = 2, and then heated on a hot plate under constant stirring until a gel was formed. The gel was calcinated at 573 K to eliminate the organic compounds and to obtain the precursor powder. Finally, the precursor powders were calcinated at 1023 K for 3 h to obtain the Nd_2O_3 nanocrystalline powder. In order to prepare Sm^{3+}:Nd_2O_3, the prepared $Nd(NO_3)_3$ was mixed with $Sm(NO_3)_3 \cdot 6H_2O$ and dissolved in distilled water and the same procedure was repeated.[21,32–35] The prepared samples are stoichiometric compounds namely $(Nd_{1-x}Sm_x)_2O_3$ with $x = 0, 0.03, 0.06$ and 0.09.

The prepared samples were tested and analysed using various techniques like PXRD, SEM, EDX, TEM, UV–Vis spectra and PL analysis. The powder X-ray diffraction (PXRD) analysis was carried out by using Bruker-AXSD8 Advance X-ray diffractometer equipped with monochromatic CuK_α radiation at 45 kV and 30 mA, in the 2θ range of 10–80° ($\lambda = 0.15406$ nm). The morphologies and composition of the prepared samples were inspected on a scanning electron microscope (SEM, VEGA 3 TESCAN, USA) equipped with an energy-dispersive X-ray spectrum (EDS, Bruker Nano, German). The transmission electron microscope (TEM, JEOL JEM-2100) studies were performed (accelerating voltage upto 200 kV). The UV–Vis absorption of the sample was recorded on a Varian Cary 5000 UV–Vis Spectrophotometer. Room temperature photoluminescence measurements were performed on a Jobin Yvon FloroMax-3 spectrofluorometer as the excitation source at 240 nm.

3. Results and discussion

3.1. Powder X-ray diffraction

The powder X-ray diffraction (PXRD) pattern of the synthesized Nd_2O_3 and Sm^{3+} doped Nd_2O_3 nanopowders are shown in Fig. 2. Using the software Powder X the diffractogram was imported and was smoothened using the adaptive smooth technique. After separating the background and subtracting it from the total profile, Cu-Kα_2 profile has been stripped out of the recorded profile. Sample peaks have been identified and indexing was done. On analysing these peaks, it was confirmed that these belong to hexagonal unit cell having $P\bar{3}m1$ space group with lattice parameters a = b = 0.3829 nm, c = 0.5998 nm. These parameters were refined to give minimum R factor (R (%) = 0.031). The crystallite size was calculated from the PXRD patterns using the Scherrer equation,

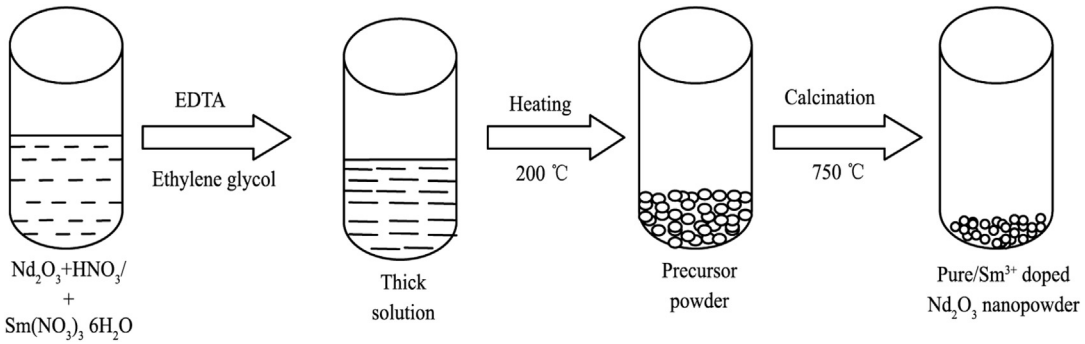

Fig. 1. Schematic diagram of modified Pechini method.

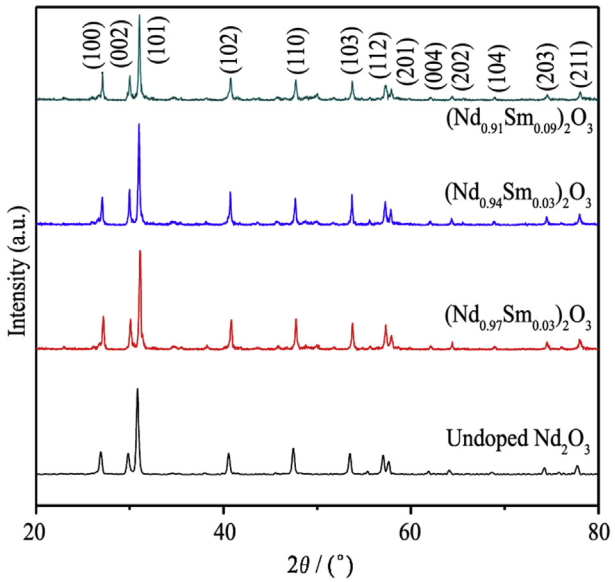

Fig. 2. Indexed PXRD pattern of undoped and Sm^{3+} doped Nd_2O_3 nanoparticles.

$$d = \frac{k\lambda}{\beta_{hkl} cos\theta_{hkl}} \quad (1)$$

where d is the average grain size of the crystallites, k is the shape factor which is 0.9 for uniform small size crystals, λ is the incident wavelength ($\lambda = 1.5406$ Å for CuKα), β is the line broadening of the diffraction peak at half the maximum intensity called full width at half maximum (FWHM), θ is the Bragg diffraction angle.[36] The crystallite size was also estimated from Williamson–Hall method.[37] The W–H equation is expressed as

$$\beta_{hkl} \cos\theta_{hkl} = \frac{k\lambda}{d} + 2\varepsilon \sin\theta_{hkl} \quad (2)$$

in which strain ε can also be calculated. The graph is plotted between $4\sin\theta_{hkl}$ and $\beta_{hkl}\cos\theta_{hkl}$ for the preferred orientation peaks of the un-doped and Sm^{3+} doped Nd_2O_3 nanoparticles with the hexagonal phase and is shown in Fig. 3. Accordingly, the slope and y-intercept of the fitted line represent the strain and the particle size respectively. The estimated crystallite sizes are in well agreement with those obtained from Scherer's formula. The values of the average crystallite size and the strain calculated from the slope of the line, for undoped and Sm^{3+} doped Nd_2O_3, are given in Table 1. It is seen that the plots showed a positive slope for pure Nd_2O_3 nanoparticles, whereas negative slopes for the Sm^{3+} doped Nd_2O_3 nanoparticles. The reason for negative strain may be due to the lattice shrinkage as seen in the estimation of lattice parameters. The strain values obtained from the W–H plots are very small and therefore have negligible effect on XRD broadening. It shows that the system goes from the unstrained lattice to a strained lattice as evidenced by the negative slope in the plot when $x = 0.03$, 0.06 and 0.09.

It allows us to anticipate some unique rearrangement of atoms and the charges due to doping effect. The transition from positive slope to negative slope itself authenticates the inclusion of Sm^{3+} ion in the host lattice at the atomic site of Nd^{3+} ion. It also results in the change in crystallite size from 34 nm when the system is pure to 25 nm when the system is doped at $x = 0.03$ level. The size gradually seems to increase but not significantly even as the dopant concentration increases. While analysing the structural parameters, the unique behaviour is also felt on refining the lattice dimensions of the unit cell. There is a significant jump between the pure and the doped system where the lattice parameters start to decrease as the dopant concentration increases. The proportional change in the lattice parameters with the dopant concentration suggests that the dopant Sm^{3+} ion has effectively replaced the host atom Nd in the lattice matrix. Although the lattice parameters are expected to decrease without any hindrance, due to the shrinking of the atomic volume at Nd^{3+} site (whose ionic radius is $r_i = 0.0995$ nm) by Sm^{3+} ($r_i = 0.0964$ nm), we see a transformation happening between $x = 0$ and $x = 0.03$ systems. This may be one of the reasons for the strain of the system at $x = 0$ to transform from being positive to a negative one when $x = 0.03$. A thorough analysis on these changes can be done from charge density distribution mapping of these systems which is done here and will be discussed in the latter.

3.2. Scanning Electron Microscopy (SEM)

Scanning Electron Microscopy (SEM) imaging has been done for examining the surface morphology of the grown nanostructures. The morphologies of the nanostructures as visualized from SEM images are shown in Fig. 4. The SEM micrographs of undoped and Sm^{3+} doped Nd_2O_3 showed small amount of agglomeration. This may be due to the strong interactions among nanoparticles owing to their high surface energy during calcination. The micrographs show agglomerate shapes as sponge-like structures. In order to get better information, it was further characterized by Transmission Electron Microscopy (TEM) so that exact morphology and size of the particles can be obtained.

3.3. Energy dispersive X-ray (EDX) analysis

To confirm the elemental composition and purity of the prepared nanopowders, the energy dispersive X-ray (EDX) analysis

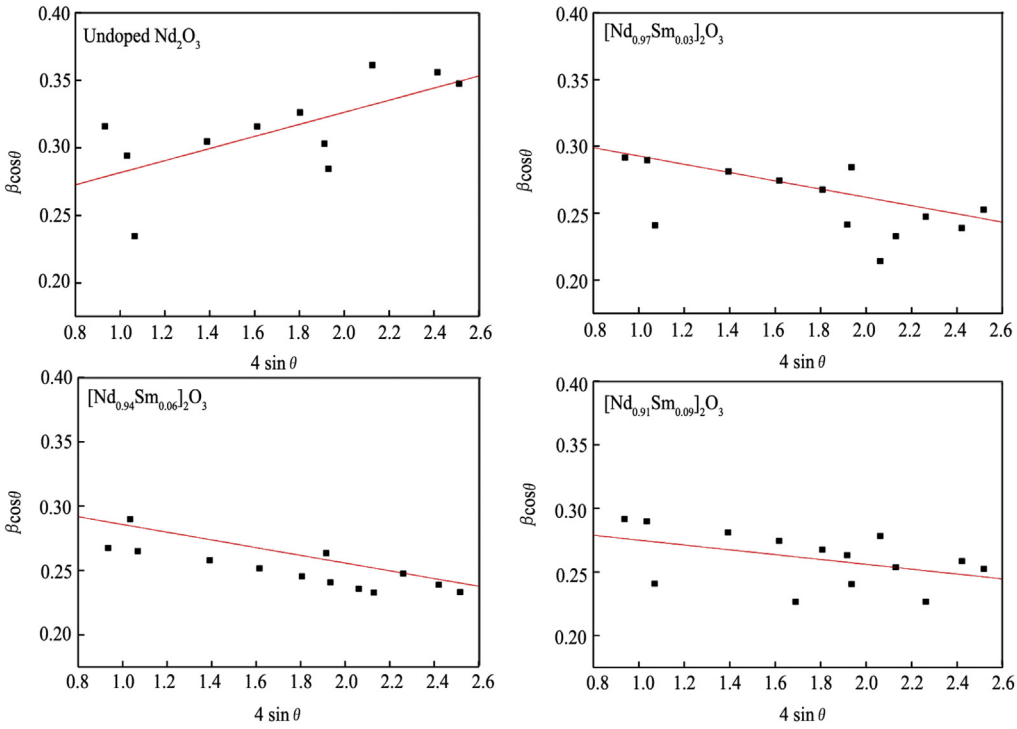

Fig. 3. W–H plots of undoped and Sm^{3+} doped Nd_2O_3 nanoparticles.

Table 1
Crystallite size of $(Nd_{1-x}Sm_x)_2O_3$.

x	Crystallite size (nm)		Strain ($\times10^{-2}$)
	Scherrer's method	W–H method	
0	32.64	34.28	4.465
0.03	31.79	25.10	−3.092
0.06	28.90	25.73	−3.0
0.09	31.79	27.62	−1.903

was carried out for Nd_2O_3 and Sm^{3+} doped Nd_2O_3 nanopowders. The EDX spectra observed for these systems are shown in Fig. 5. The elements Nd and O were detected in the peaks in the spectra of the energy dispersive X-ray (EDX) analysis of pure Nd_2O_3 nanopowders [Fig. 5(a)] and in the EDX spectra of Sm^{3+} doped Nd_2O_3 nanopowders [Fig. 5 (b–d)], presence of Nd, Sm and O was observed. The results show that pure and Sm^{3+} doped Nd_2O_3 nanopowders were successfully synthesized. The analysis confirmed that there was no presence of other elements from the organic compounds which were initially used in the synthesis.

3.4. Transmission Electron Microscopy (TEM)

In order to determine a more precise particle size of the prepared nanomaterials, the powders were examined at a smaller scale using transmission electron microscopy (TEM). The TEM images of the undoped and Sm^{3+} doped Nd_2O_3 nanoparticles are shown in Fig. 6. TEM results clearly show that the particles are in nanoscale regime which is consistent with the results of XRD analysis. The selected area electron diffraction (SAED) patterns (Fig. 7) show a ring structure with dots, indicating the crystalline nature and reduced size of the particles. The pattern can be indexed to the hexagonal phase of Nd_2O_3, which is also in good agreement with XRD results. The particle size obtained from TEM is in the range 25–35 nm, as found using Scherrer's equation.

3.5. UV–Vis spectral analysis

The UV–Vis absorption spectrum of pure and Sm^{3+} doped Nd_2O_3 nanoparticles are shown in Fig. 8(a). The absorbance is expected to depend on various factors like band gap, oxygen deficiency, surface roughness and impurity centres. The spectra exhibit prominent maximum absorption band at approximately 240 nm corresponding to band gap of 5.16 eV. This maximum absorption arises due to the photo excitation of electrons from lowest unoccupied molecular orbital (LUMO) to highest occupied molecular orbital. The absorption bands are ascribed to charge transition[38,39] as follows:

240 nm $Nd^{3+}: {}^4I_{9/2} \rightarrow {}^2F_{7/2} + {}^2F_{5/2} + Sm^{3+}$
$: {}^6H_{5/2} \rightarrow {}^2G_{9/2} + {}^2D_{3/2} + {}^2K_{13/2} + {}^2I_{11/2}$

294 nm $Nd^{3+}: {}^4I_{9/2} \rightarrow {}^2D_{5/2} + {}^2H_{11/2} + {}^2D_{3/2} + Sm^{3+}$
$: {}^6H_{5/2} \rightarrow {}^4F_{9/2} + {}^2K_{13/2}$

356 nm $Nd^{3+}: {}^4I_{9/2} \rightarrow {}^4D_{3/2} + {}^4D_{5/2} + {}^2I_{11/2} + {}^4D_{1/2} + Sm^{3+}$
$: {}^6H_{5/2} \rightarrow {}^4H_{7/2} + {}^4D_{5/2} + {}^4D_{3/2}$

434 nm $Nd^{3+}: {}^4I_{9/2} \rightarrow {}^2P_{1/2} + Sm^{3+}: {}^6H_{5/2} \rightarrow {}^4I_{15/2} + {}^2G_{9/2}$

475 nm $Nd^{3+}: {}^4I_{9/2} \rightarrow {}^2G_{9/2} + {}^2D_{3/2} + {}^4G_{11/2} + {}^2K_{15/2}$
$+Sm^{3+}$
$: {}^6H_{5/2} \rightarrow {}^4I_{11/2}$

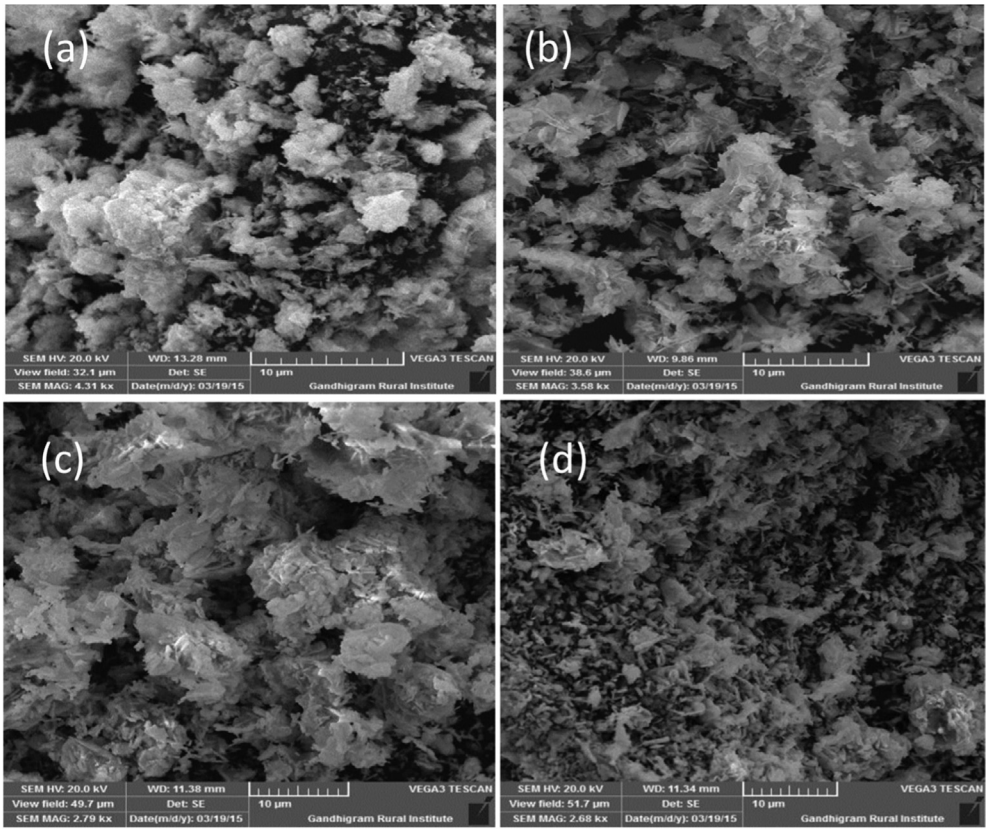

Fig. 4. SEM images of $(Nd_{1-x}Sm_x)_2O_3$, (a) $x = 0$, (b) $x = 0.03$, (c) $x = 0.06$ and (d) $x = 0.09$.

529 nm $Nd^{3+}: {}^4I_{9/2} \rightarrow {}^4G_{9/2} + {}^4G_{7/2} + {}^2K_{13/2} + Sm^{3+}$: ${}^6H_{5/2} \rightarrow {}^4F_{3/2}$

597 nm $Nd^{3+}: {}^4I_{9/2} \rightarrow {}^4G_{5/2} + {}^2G_{7/2}$

689 nm $Nd^{3+}: {}^4I_{9/2} \rightarrow {}^4F_{5/2}$

753 nm $Nd^{3+}: {}^4I_{9/2} \rightarrow {}^4F_{7/2} + {}^4S_{3/2}$

The absorption edge of different samples varies as the concentration of Sm^{3+} in the Nd_2O_3 nanoparticles varies. The absorption edge is blue shifted with respect to the bulk absorption edge appearing at 270 nm. The optical band gap energy (E_g) of the samples was estimated from UV Diffuse reflectance data by transforming it into a function of reflectance as proposed by Kubelka–Munk.[40] The reflectance was converted into Kubelka–Munk function, $F(R)$, using the relation:

$$F(R) = (1 - R)^2 \Big/ 2R \quad (3)$$

where R is the reflectance of the sample with respect to a reference at each wavelength. The Kubelka–Munk plot for determining optical band gap energy of the undoped and Sm^{3+} doped Nd_2O_3 nanoparticles is shown in Fig. 8(b). It is plotted using the *nth* power of the function of reflectance $F(R)h\nu$ and $h\nu$, the photonic energy. Considering direct electronic transitions in Nd_2O_3[41] the value of n is taken as 2 for the allowed transitions. The optical energy band gap is determined by extrapolating the linear portion of the plot to the energy axis. The estimated E_g values of undoped Nd_2O_3, Nd_2O_3:3% Sm, Nd_2O_3:6%Sm, Nd_2O_3:9%Sm were 5.05, 5.13, 5.01 and 5.1 eV respectively. This variation in the values might be due to structural disorders in the lattice which changes the intermediate energy level distribution within the band gap. It can be said here that the strain induced by the dopant Sm^{3+} ion affects the band gap of the system too.

3.6. Photoluminescence studies

The photoluminescence spectrum of the synthesized Nd_2O_3 and Sm^{3+} doped Nd_2O_3 nanoparticles obtained when the excitation was monitored at 240 nm wavelength is shown in Fig. 9. It is observed that increasing the doping concentration of Sm^{3+} ions had no influence on position of the emission peaks, except for considerably enhancing the relative intensity. The PL spectra show a broad series of emission bands. The spectrum showed emissions at 347, 375, 421, 442, 473, 485 and 530 nm corresponding to Nd^{3+} ion.[36] The emissions at 397 nm and 560 nm correspond to that of Sm^{3+} ion. The optimal doping molar concentration of Sm^{3+}, which generated the maximum intensity, was 6%. When the Sm^{3+} concentration was greater than 6%, the concentration quenching phenomena caused the PL emission intensity to decrease. The maximum intensity at 397 nm is due to the presence of Sm^{3+} ion and due to the energy transfer between ${}^4K_{11/2} \rightarrow {}^6H_{5/2}$ of Sm^{3+} ion which arises due to the s = 6 type electrostatic dipole–dipole interaction. The observed dipole–dipole interaction could possibly be the evidence of above said electronic transition that produced the high intense photoluminescence peak at $x = 0.06$ concentration. The transitions in the UV region can be ascribed due to the singly ionized oxygen vacancies in Nd_2O_3.[25] It is reported[41,42] that the broad UV emission can also take place owing to the

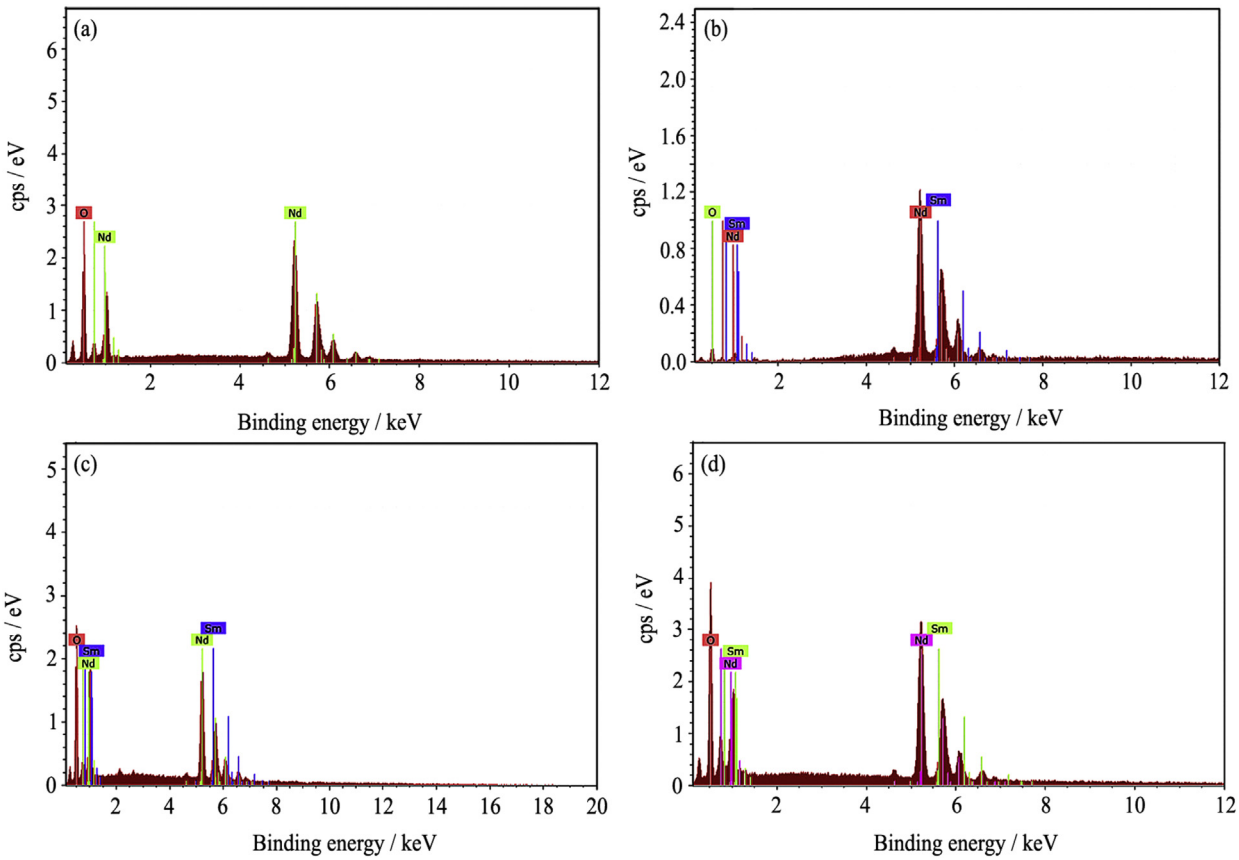

Fig. 5. EDX pattern of $(Nd_{1-x}Sm_x)_2O_3$, (a) $x = 0$, (b) $x = 0.03$, (c) $x = 0.06$ and (d) $x = 0.09$.

recombination of free exciton through an exciton–exciton collision process. The visible emission was due to recombination of photo-generated hole with an electron occupying the oxygen vacancy and also due to the presence of surface defects like Schottky and Frenkel that exists in the lattice.

The purity in colour of the emission of pure and Sm^{3+} doped Nd_2O_3 nanoparticles can be found out by CIE (Commission International del'Eclairage) chromaticity coordinates. The corresponding colour of the samples were marked in the CIE chromaticity diagram according to their *X* and *Y* coordinates and is shown in Fig. 10. The colour coordinates of the samples which were estimated from the photoluminescence spectra are (0.1674, 0.1670), (0.1645, 0.1591), (0.1781, 0.1597) and (0.1693, 0.1648) for undoped Nd_2O_3, Nd_2O_3:3%Sm, Nd_2O_3:6%Sm, Nd_2O_3:9%Sm respectively and is shown in the inset of Fig. 10. CIE diagram confirms that the samples produce emissions exactly in the blue region and this phosphor material can be effectively used in the field of colour displays.

3.7. Rietveld analysis

The arrangement of charges in the host lattice of the chosen system is one of the most important criteria in determining the properties of any material. X-ray diffracted structure factors give all the informations on the distribution of charges between the atoms and in the lattice. It is possible from this to investigate the way in which the charges distribute themselves under a particular environment and thus throws more light on the behaviour of the system. The experimental powder XRD profile is used to get the detailed X-ray diffraction information and to extract charge density. The Rietveld refinement[43] is a method, devised by Hugo Rietveld, for the structural characterization of crystalline materials, uses the least squares approach to refine an observed X-ray diffraction profile pattern until it matches with the calculated profile while getting accurate information of the structure. In this technique, structural parameters, lattice parameters, peak shift, background profile shape and the preferred orientation are refined. The basic principle of the Rietveld method is to minimize the difference between the theoretically modelled profile and the observed one. In this method, the profile intensities obtained from step-scanning measurements of the powders allow to estimate an approximate structural model for the real structure. It was performed for all the data sets of $(Nd_{1-x}Sm_x)_2O_3$ using the software package JANA 2006[44] which employs Rietveld technique. The lattice parameter, fractional atomic coordinates, atomic displacement parameters, and the occupation factors were obtained from whole powder diffraction patterns. Twenty five terms of Legendre polynomials were used to describe the background. The peak shape function was of pseudo-Voigt type introducing Gaussian type profile parameters (*Gu*, *Gv*, *Gw*) and Lorentzian type parameters (*Lx*, *Ly*). The fitting parameters (*Rp*, *wRp* and *GoF*) show a good agreement between the refined and observed XRD patterns for the chosen systems. The refined lattice, thermal and structure factors are presented as Tables 2–4. The results confirm that the prepared undoped and Sm^{3+} doped Nd_2O_3 has a hexagonal structure and belonged to $P\bar{3}m1$ space group. The isotropic and anisotropic thermal parameters evaluated from the refinement is presented as Table 3 where the addition of Sm^{3+} ion at the site of Nd^{3+} introduces a sudden increase in the vibrational amplitude (U_{iso}) and then it decreases gradually as we increase the dopant concentration. The jerky behaviour is primarily due to the strain introduced into the system which relaxes the lattice in order to accommodate Sm^{3+} ion

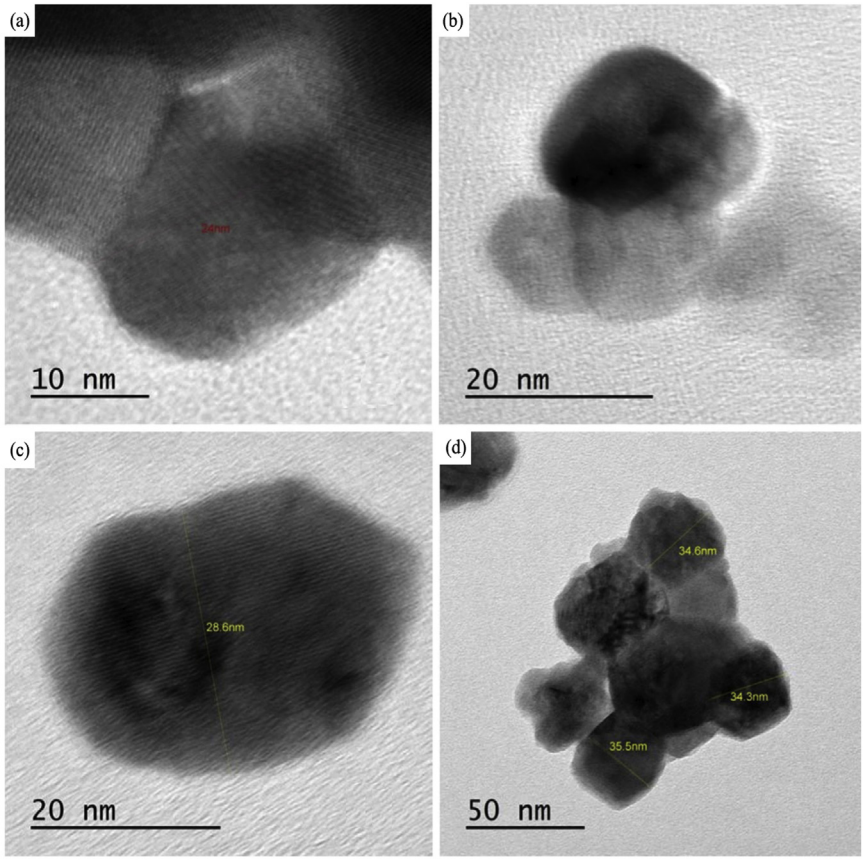

Fig. 6. TEM images of the $(Nd_{1-x}Sm_x)_2O_3$ nanoparticles (a) $x = 0$, (b) $x = 0.03$, (c) $x = 0.06$ and (d) $x = 0.09$.

into it, but the decreasing behaviour of U_{iso} and other parameters U_{11}, U_{22} and so on allowed us to look into the very formation of sesquioxide nanosystems. Evidently, the entropy of formation of sesquioxides like Nd_2O_3 and Sm_2O_3 as observed[45] reveals that the entropy of formation ΔS for Sm_2O_3 is 36.1 calgfw^{-1} K^{-1} which is lower than that of Nd_2O_3 ($\Delta S = 37.9$ calgfw^{-1} K^{-1}). Hence when Sm^{3+} ion is forcefully introduced into the host system, the doping process will invariably reduce the entropy of the system and will bring the system into an order. This will naturally result in the decrease in the isotropic and anisotropic thermal parameters as evidenced from Table 3.

3.8. Charge density analysis

The Rietveld refinement technique is primarily used for extracting structural and profile parameters. The accurate refined structure factors obtained can be further used for the construction of charge density in the unit cell using maximum entropy method. The structure factors derived using Rietveld technique should be subjected to Bayesian statistical analysis to reduce the noise in the data so that any of the deviations from reality that may occur in our calculations are largely reduced. The Maximum Entropy Method (MEM) is a standard tool, proposed by Collins[46] which is used to estimate the accurate charge density distribution from phase factors derived from experimentally determined structural factors. According to him, MEM is an iterative method based on constrained entropy maximization which constructs the electron density even from very few available X-ray diffraction data. MEM is one of the methods which handles the uncertainty properly using the concept of entropy. The principle of MEM is to attain the electron density distribution, consistent with the observed structure factors and results in maximizing the uncertainties.[46] Syed Ali et al. have given the detailed methodology and algorithm of the MEM procedure in their work on ZnSe and PbSe.[47] Charge density enumerated using MEM is real and positive everywhere because of their statistical approach. It provides an accurate picture of distribution of charges especially in the valence region and therefore it is used for analysing the bonding features and other structure based properties. Lately, the combination of MEM/Rietveld method was proposed by Takata in 2008 and it was applied to nanosystems.[48–51] The same approach used by Takata et al. is employed here too where JANA 2006 and PRIMA softwares[44,52] are used for the evaluation of charge density and the estimated charge density distribution in the unit cell are visualized using VESTA.[53]

The phase factors derived from the Rietveld refinement (Table 4) were used for MEM refinements. The MEM refinements were carried out by dividing the unit cell into 64 × 64 × 100 pixels so that it matches the scaling defined by the lattice dimensions. The initial electron density at each pixel is fixed uniformly at $F_{000}/V = 1895$ e/nm^3, where F_{000} is the total number of electrons in the unit cell and V is the cell volume. According to Collins, the MEM electron density at the ith pixel is

$$\rho(\boldsymbol{r}_i) = \tau(\boldsymbol{r}_i)\exp\left[\left(\frac{\lambda F_{000}}{N}\right)\sum[1/\sigma(k)]^2|F_{Obs}\,(\boldsymbol{k}) - F_R(\boldsymbol{k})|\exp(-2\pi j\,\boldsymbol{k}.\boldsymbol{r})\right] \quad (4)$$

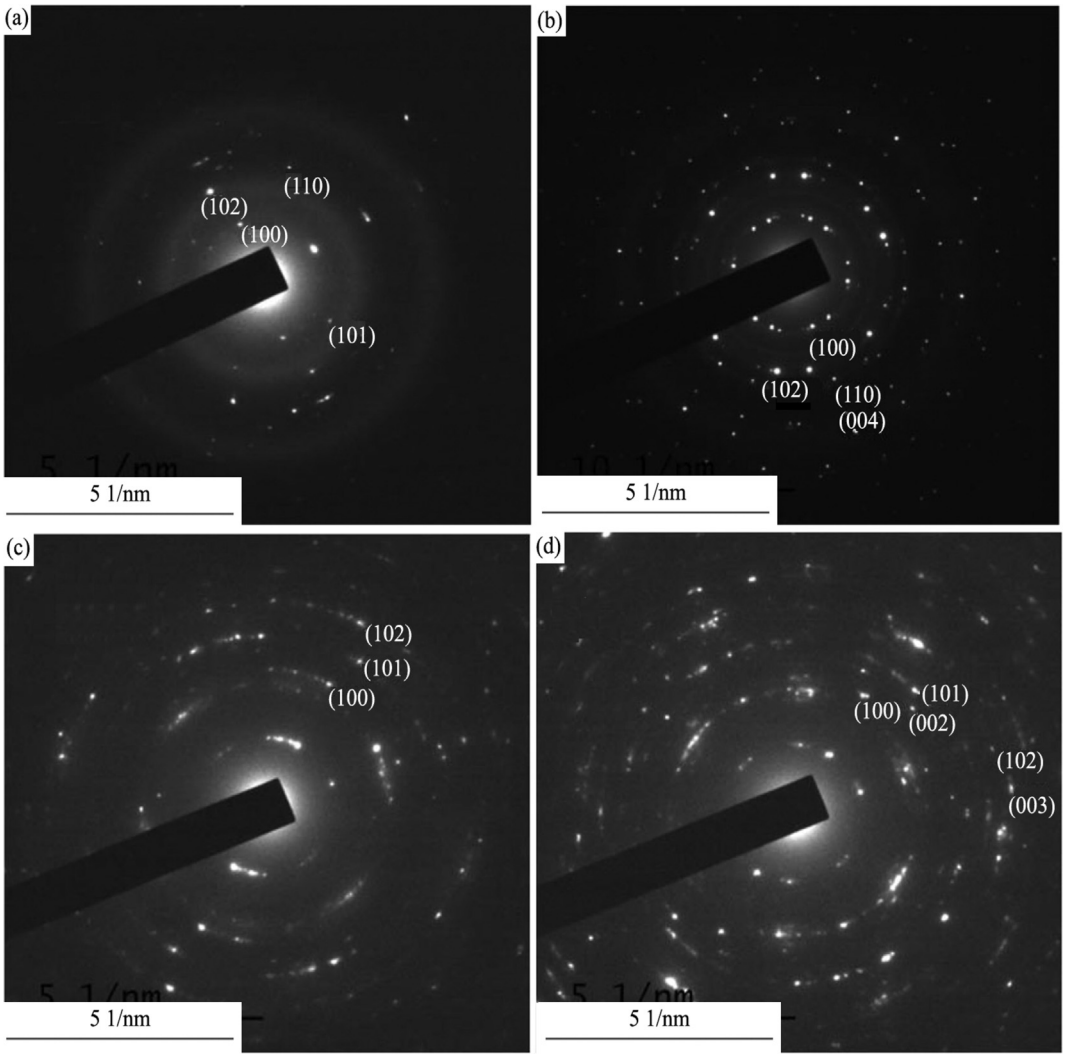

Fig. 7. SAED pattern of $(Nd_{1-x}Sm_x)_2O_3$ nanoparticles. (a) $x = 0$, (b) $x = 0.03$, (c) $x = 0.06$ and (d) $x = 0.09$.

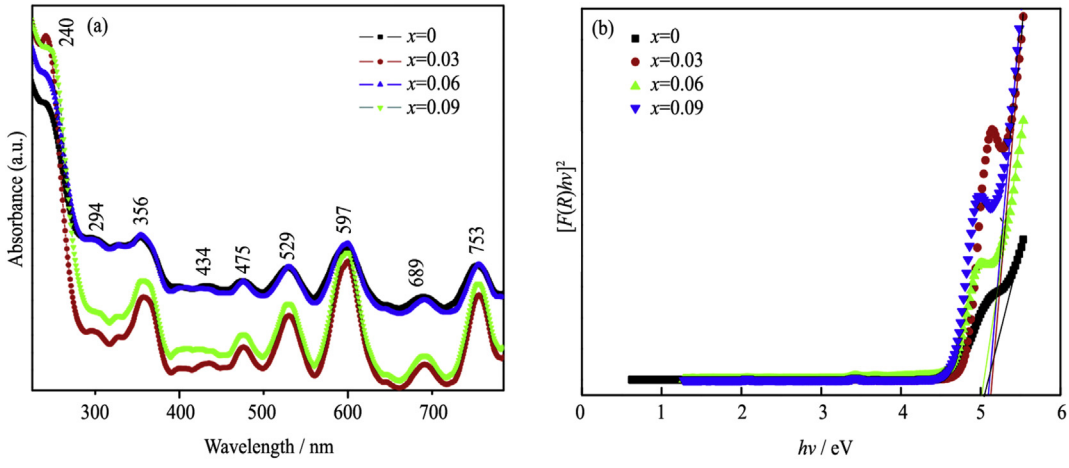

Fig. 8. **(a)** UV–Vis absorption spectra and **(b)** Energy band gap of $(Nd_{1-x}Sm_x)_2O_3$ nanoparticles.

where $\tau(\boldsymbol{r}_i)$ is the prior electron density, N is the number of reflections, λ is the Lagrange's multiplier and F_R is the structure factor calculated from Rietveld refinement. The Lagrangian parameter (λ) is suitably chosen so that the convergence criterion $C = 1$ is reached after a minimum number of iterations where the weak constraint is defined as

$$C = (1/N)\sum[F_{Obs}(\boldsymbol{k}) - F_{Cal}(\boldsymbol{k})]^2 \Big/ \sum \sigma(\boldsymbol{k})^2 \quad (5)$$

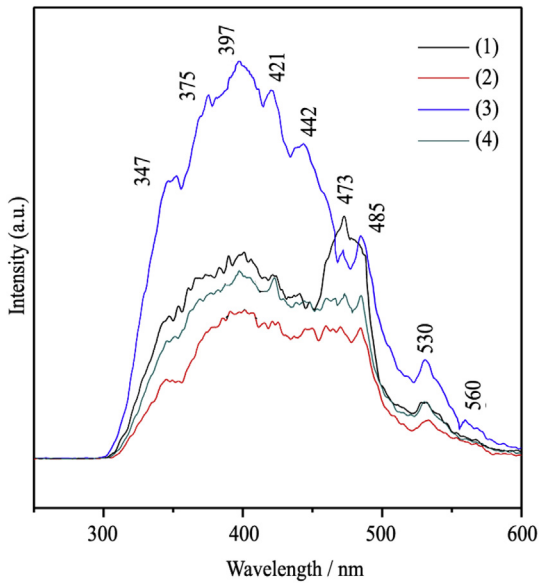

Fig. 9. PL spectra of $(Nd_{1-x}Sm_x)_2O_3$ nanoparticles. (1) $x = 0$, (2) $x = 0.03$, (3) $x = 0.06$ and (4) $x = 0.09$.

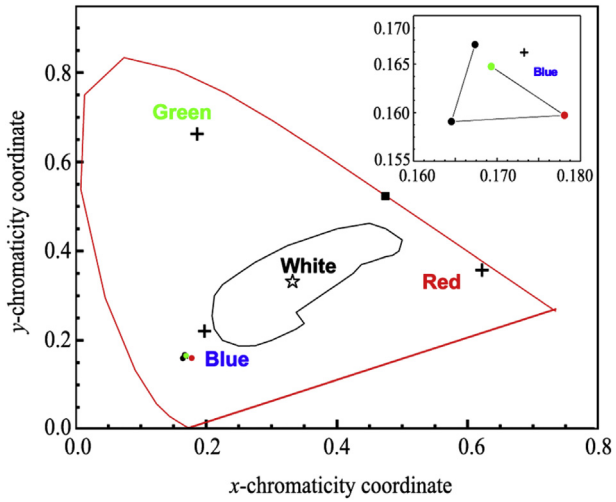

Fig. 10. The CIE 1931 colour chromaticity diagram of $(Nd_{1-x}Sm_x)_2O_3$ nanoparticles. (Inset: Enlarged portion of the obtained colour coordinates.)

When $\sigma(k)$, F_{Obs} $(\boldsymbol{k})$ and the Lagrange's multiplier λ are given, $\rho(r_i)$ could be obtained which is the desired MEM estimate for $\rho_{mem}(r_i)$, the electron density distribution. Estimation of charge density is done using $F_R(\mathbf{k})$ which is replaced by $F_{mem}(\mathbf{k})$, structure factor determined by MEM, after every iteration. For the numerical MEM computations, the software package PRIMA was used. For the 2D and 3D representation of the electron densities, the program VESTA package was used. The parameters used in MEM refinement are also given in Table 2.

In order to visualize the influence of dopant at the valence region, the three dimensional arrangement of the charges in the unit cell was drawn at an isosurface level of 1150 e/nm^3 for all the prepared samples and is shown as Fig. 11, which visualises the electron clouds between Nd and O. The 3-D pictures [Fig. 11] show the expected change in the charge arrangement of both Nd^{3+} and O^{2-} ions. They seem to get involved in the bonding process more vigorously as the dopant concentration increases. For the pure case the bonds appear to be between two different inverted

Table 2
Refined parameters.

Parameters	$x = 0$	$x = 0.03$	$x = 0.06$	$x = 0.09$
I. Structure refinement				
a = b (10^{-1} nm)	3.8278	3.8335	3.8315	3.8287
c (10^{-1} nm)	5.9931	6.0025	5.9990	5.9969
α = β	90	90	90	90
γ (°)	120	120	120	120
V (10^{-3} nm^3)	76.05	76.39	76.27	76.13
ρ(gm/cm^3)	7.347	7.322	7.342	7.363
R_F (%)	1.46	1.98	1.59	2.9
wR (%)	1.24	2.09	1.64	2.75
GOF	1.06	1.89	1.85	1.94
II. MEM refinement				
Number of reflections (N)	29	29	28	28
Prior density, $\tau(r_i)$ (10^3 e/nm^3)	1.893	1.887	1.866	1.896
Lagrange parameter (λ)	0.0286	0.0317	0.0334	0.0488
Number of iterations	187	218	235	389
R_{obs} (%)	2.4325	2.606	2.678	4.01
wR_{obs} (%)	0.2663	0.267	0.262	2.63
Resolution (10^{-1} nm/pixel)	0.0598	0.0599	0.0599	0.0598

Table 3
Refined non-zero isotropic and anisotropic thermal parameters.

Atoms	x	U_{iso} (10^{-2} nm^2)	U_{11}	U_{22}	U_{33}	U_{12}
Nd	0	0.0377	0.0375	0.0375	0.0379	0.0188
Nd/Sm	0.03	0.0621	0.0626	0.0626	0.0610	0.0313
	0.06	0.0425	0.0423	0.0423	0.0429	0.0212
	0.09	0.0368	0.0365	0.0365	0.0376	0.0182
O1	0	0.0538	0.0458	0.0458	0.0699	0.0229
	0.03	0.0987	0.1475	0.1475	0.0012	0.0738
	0.06	0.0940	0.1366	0.1366	0.0088	0.0683
	0.09	0.0490	0.0889	0.0889	−0.0307	0.0445
O2	0	0.3228	0.0268	0.0268	0.0433	0.0134
	0.03	0.1165	0.2082	0.2082	−0.0669	0.1041
	0.06	0.0401	0.0759	0.0759	−0.0316	0.0379
	0.09	0.0107	0.0410	0.0410	−0.1143	0.0205

dipoles made by Nd_1-O_1 and Nd_2-O_2. The individual bonds Nd–O seem to be more of ionic while the dipoles seem to interact along O_1-Nd_2 and Nd_1-O_2 directions. As the doping concentration increases, the dipole–dipole distances (d_{O1-Nd2}, d_{Nd1-O2}) increases. At the same time, the individual bonds (Nd–O) attempt to strengthen their interaction as evidenced by the overlapping of charge density as doping concentration increases. Moreover the dipoles seem to attract themselves between the possible non nuclear maxima (NNM) as seen in Fig. 11. Thus the doping of Sm^{3+} ion completely changes the charge distribution scenario and their interactions. To understand them in a qualitative way, the cross section of the unit cell is drawn along (220) plane choosing the contour levels ranging from 0.5 to 1000 e/nm^3 at an interval 50 e/nm^3 and is shown in Fig. 12. Interestingly, we can understand why the system has gone from the positively strained one when $x = 0$ and negatively strained one when the system is doped. In Fig. 12 (a), the ground state mapping of Nd_2O_3 enables us to see the inverted dipole containing Nd_1-O_1 and Nd_2-O_2 and their interactions. Evidently, the individual bonds are much stronger as seen in the picture where the charge accumulation is found to be more between Nd–O individual bonds than between the dipoles. The Newton–Raphson search for the (3, −1) bond critical point (BCP) showed that the BCPs are placed along an outwardly curved (convex) bond path. The surprise transformation of the charge density distribution when Sm^{3+} ion is doped can be seen in Fig. 12(b). In this it is very clearly depicted that the bond path between Nd_1-O_1 and Nd_2-O_2 has changed from a positive curvatured one to a negative curvatured one and hence the BCPs are drifted inward. The directions of the dipole–dipole interactions

Table 4
Structural factors for $(Nd_{1-x}Sm_x)_2O_3$.

h	k	l	$x = 0$		$x = 0.03$		$x = 0.06$		$x = 0.09$	
			F_o	F_c	F_o	F_c	F_o	F_c	F_o	F_c
1	0	0	46.7222	46.8923	46.162	46.6187	47.3219	47.611	45.2404	46.8701
0	0	2	87.1561	87.2375	79.7939	81.1154	87.273	86.7906	80.3742	82.0894
1	0	1	61.8964	62.0263	59.6169	60.3951	63.0021	63.4732	64.3226	64.2015
1	−1	1	78.5835	78.7484	73.0854	74.0393	77.2728	77.8506	76.3967	76.2529
1	0	2	35.5543	35.3885	30.9549	30.8015	32.4707	32.2387	28.8989	28.8159
1	−1	2	53.466	53.2166	51.2704	51.0164	59.0738	58.6517	62.4273	62.248
2	−1	0	81.6547	81.4126	66.9242	67.1515	79.5738	79.4932	76.8298	76.6165
1	0	3	59.5377	59.4869	53.5357	53.463	61.7233	61.8017	64.7524	64.817
1	−1	3	54.8559	54.8091	43.8661	43.8065	51.4603	51.5256	40.7543	40.795
2	0	0	29.2084	29.9925	21.8926	23.9064	28.4325	29.117	24.0128	26.0933
2	−1	2	57.9592	58.2113	49.7802	50.6197	59.512	60.5855	55.8212	56.8974
2	0	1	51.5577	52.2914	38.7486	38.5671	49.868	50.4547	44.9453	45.1037
2	−2	1	42.9915	43.6032	39.8903	39.7035	45.0479	45.5779	45.2574	45.4169
0	0	4	54.0497	54.5411	41.0876	43.7317	51.1466	49.6081	54.6649	49.6579
2	0	2	32.0787	33.9732	27.8247	27.8813	35.7789	33.5397	37.0351	39.0325
2	−2	2	24.3451	25.7828	17.8701	17.9065	28.8757	27.0685	20.8011	21.9229
1	0	4	15.2377	16.4279	2.8089	2.8591	3.0828	3.2653	10.5228	11.3342
1	−1	4	24.2427	26.1363	25.213	25.664	31.9139	33.8035	28.9932	31.2289
2	0	3	38.4926	39.6137	26.0136	25.4076	38.9469	38.4856	28.646	25.7802
2	−2	3	40.9418	42.1342	34.2987	33.4997	43.369	42.8553	49.8311	44.846
3	−1	0	20.2257	22.2123	18.2482	17.4233	22.0985	23.4006	19.8424	20.4129
3	−2	1	39.7889	39.4434	29.8884	28.0123	42.2378	41.3556	38.8716	37.3503
3	−1	1	32.3036	32.0231	27.4701	25.7458	34.0799	33.3681	34.0985	32.8096

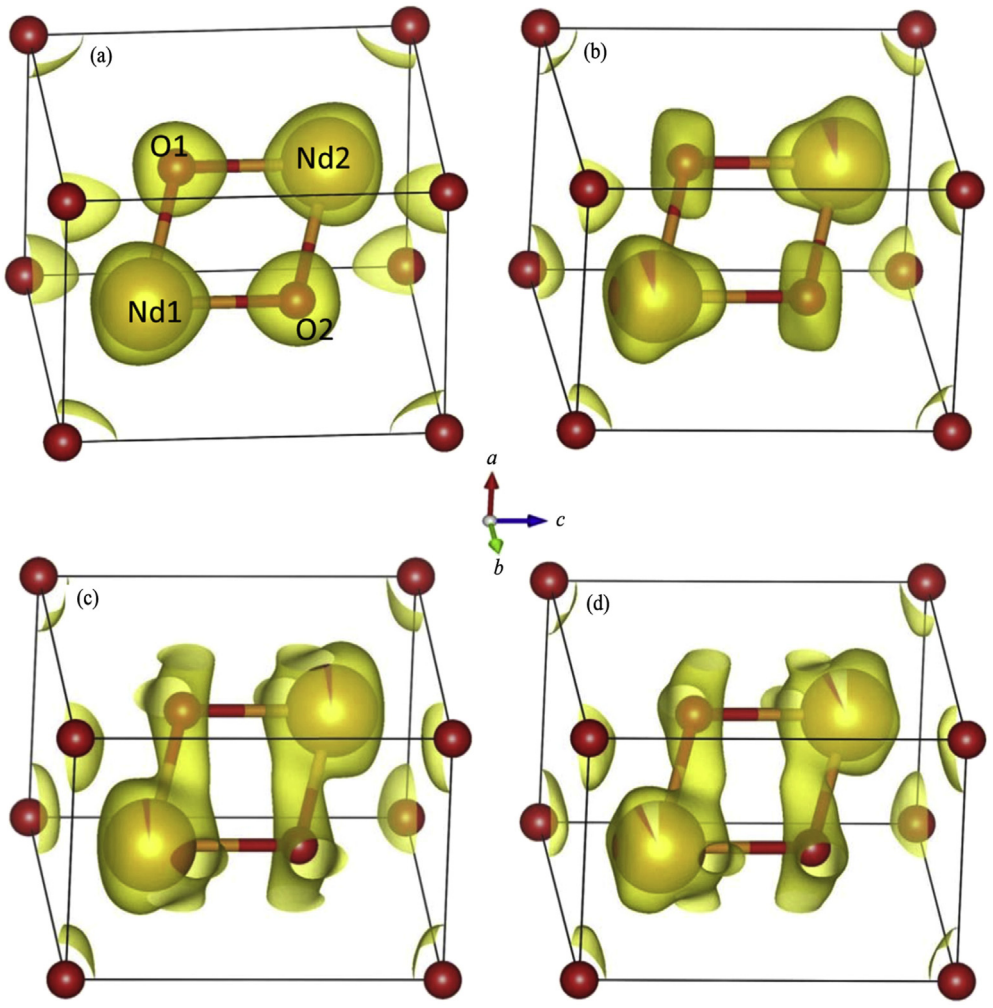

Fig. 11. Three-dimensional charge density distribution in $(Nd_{1-x}Sm_x)_2O_3$ nanoparticles (a) $x = 0$, (b) $x = 0.03$, (c) $x = 0.06$ and (d) $x = 0.09$. The isosurface level is 1150 e/nm^3.

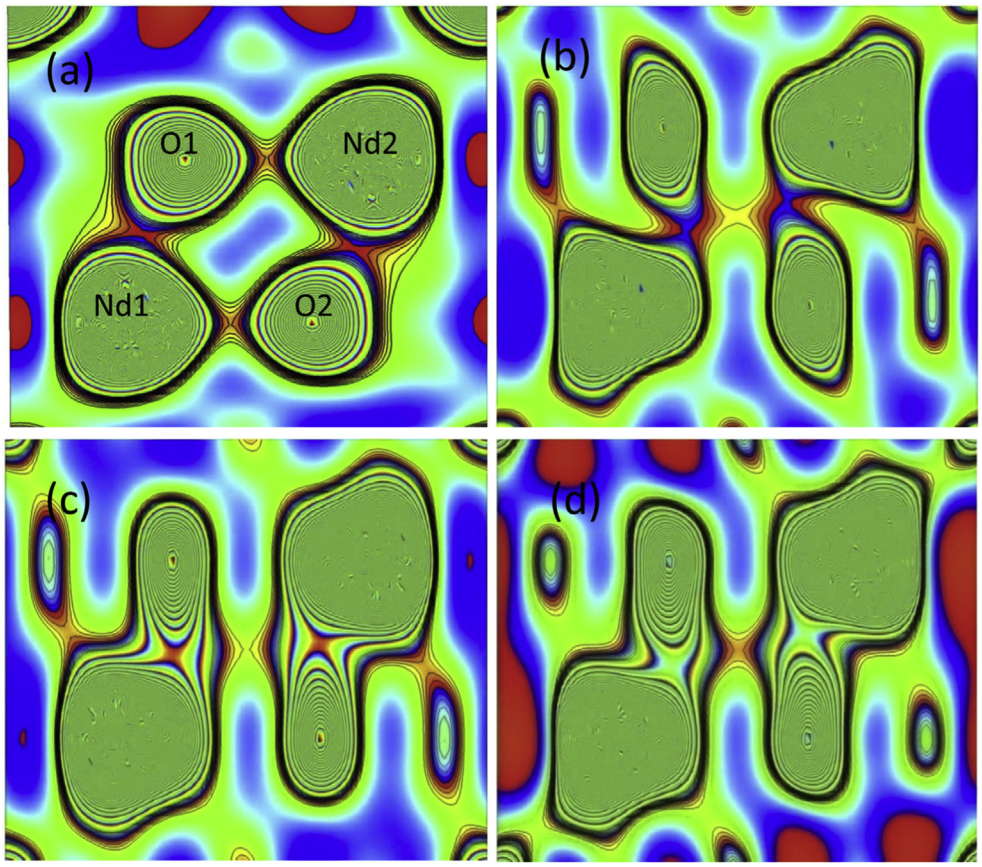

Fig. 12. Two-dimensional MEM electron density map of $(Nd_{1-x}Sm_x)_2O_3$ nanoparticles along (220). (a) $x = 0$, (b) $x = 0.03$, (c) $x = 0.06$ and (d) $x = 0.09$.

changed in a more pronounced manner and now it is centred at a non-nuclear maxima (NNM) created between BCP_1 and BCP_2 (See Fig. 12(c) and (d)). A schematic diagram of the bond path before and after doping along with BCPs and NNM is shown in Fig. 13. The cross sections drawn for $x = 0.06$ and $x = 0.09$, show a little ordered charge arrangement while strengthening the interactions at BCPs and NNM. Hence the doping of Sm^{3+} ion into the host Nd^{3+} matrix seem to have completely shaken the charge environment in the lattice and redistributed it in its own way. This behaviour is clearly understood from the accurate all positive entropy maximized electron density. Maximum entropy method has once again proved to be a tool that can bring intricate details of any system and can throw more light on the charge rearrangement of any system under certain environmental conditions.

To quantify the observations, we have enumerated the charge density at BCPs and NNM and also measured the straight distances between the atoms and the BCPs and are presented in Table 5. All the arguments we have put forth have been authenticated by the values shown in Table 5. When the doping is increased from $x = 0$ to $x = 0.09$, it should be understood that the distance between Nd and the BCP has been authenticated by the values shown in Table 5. When the doping is increased from $x = 0$ to $x = 0.09$, it should be understood that the distance between Nd and the BCP has gradually increased and has attained the maximum at $x = 0.09$ while the same behaviour has happened for d_{O-BCP}. But the change in the curvature of the bond path between Nd–O from being positive to negative has resulted in a sudden jump in the interaction between Nd and O and hence the charge density accumulation at BCP shoots up from 73.2 e/nm^3 to 1930.6 e/nm^3. The resultant induced dipole–dipole interaction will have an influence in the dielectric function of the material which will invariably reflect on the optical property of the system. Such a change in the chosen material is very pronounced as evidenced from the charge density mapping and has to be investigated further.

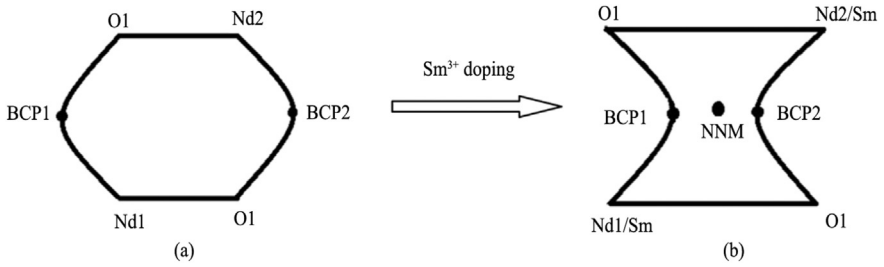

Fig. 13. Schematic diagram of the bond path (a) before and (b) after doping.

Table 5
(3,−1) BCPs, NNMs and their charge densities.

	$x = 0$	$x = 0.03$	$x = 0.06$	$x = 0.09$
$d_{Nd1-BCP1}(10^{-1}$ nm)	1.15	1.16	1.18	1.36
$\rho_{BCP1}(10^{-3}$ e/nm^3)	0.7322	1.9306	1.5919	0.7032
$d_{O1-BCP1}(10^{-1}$ nm)	1.04	1.13	1.23	1.32
$d_{Nd2-BCP2}(10^{-1}$ nm)	1.14	1.16	1.19	1.35
$d_{O2-BCP2}(10^{-1}$ nm)	1.02	1.14	1.22	1.33
$d_{BCP1-BCP2}(10^{-1}$ nm)	2.4	1.77	1.66	1.32
$\rho_{NNM}(10^{-3}$ e/nm^3)	0.2064	0.4948	0.5209	0.5910

An effect of the dipole–dipole interaction and the accumulation of charges at the BCP of Nd–O with respect to the doping concentration should result in the decrease in the band gap energy (E_g). Any interaction between the neighbouring atoms resulting in the accumulation of the charges between the bonds at BCP, will result in the system going towards conducting state. Any system that goes from a less conducting state (insulating) to a more conducting state (metallic) will have its energy gap reducing. And thus the charge density between the neighbours can be a signature ascertaining the conducting state of the system. Any strong or overlapping interactions should result in the increase in the conductivity of the system resulting in the reduction of the band gap energy. The reported decreasing trend in the values of E_g of the prepared systems is authenticated by the results of charge density enumeration. In order to bring the system to an order, the charge density at BCP again reduces as x increases and attains a lower value at $x = 0.09$. The change in the curvature from positive to negative is also evidenced by the distance measured by the between BCP_1 and BCP_2. The BCPs were distant apart when $x = 0$ and due to the reverse in the curvature of the bond paths, the distance shrinks to 1.77 and then to 0.132 nm as x goes from 0.03 to 0.09. The change in the curvature and the resultant dipole–dipole interaction resulted in the creation of non-nuclear maxima along BCP_1–BCP_2. The strength of the dipole–dipole interaction is gauged by the charge density at NNM and it seemed to increase uniformly as the dopant concentration increases. And hence it can be concluded that the dopant Sm^{3+} ion induces a change in the lattice and the charge arrangement that leads to an ordered system as the dopant concentration increases. The jerky behaviour of the Nd_2O_3 system when Sm^{3+} ion is doped is indeed very unique and should be investigated further on by other scientific methods possible.

Concentration quenching will give us the maximum limit of doping concentration into the host system. Thus the intensity of photoluminescent emission will reach the maximum around $x = 0.06$ where the doping concentration has reached the maximum value. Any more addition of the dopant will only introduce more lattice strain than contributing to the property of the system. And hence any more forceful addition of the dopant will not influence charge environment and also the bonding process. Thus the concentration quenching affects only the PL intensity but not the charge density at BCP (see Table 5). The photoluminescence (PL) effect and the creation of exciton levels are indeed the result of the interaction between the dipoles and the creation of NNM between the BCPs. The strengthening of the individual Nd–O bonds and between dipole–dipole resulted in the lowering of E_g as x increases from 0.03 to 0.06 where concentration quenching is achieved. This resulted in the PL intensity being very high for $x = 0.06$ at the excitation of 240 nm and also the creation of excitons at the nearby range. Thus the charge density picture enables us to see and reason out the spectral behaviour of the system. Thus the mapping of charge density allows us to understand the physical property of the system in a given environment. Such studies strengthen the claim that the charge density studies should be done for any system as it throws more light on the system than itself.

4. Conclusion

Nanostructured Nd_2O_3 and Sm^{3+} doped Nd_2O_3 nanophosphors were successfully synthesized at 750 °C for the first time using modified Pechini method. X-ray powder diffraction studies of the synthesized nanocrystals reveals its hexagonal structure with $P\bar{3}m1$ space group and lattice parameters $a = b = 0.3829$ nm, $c = 0.5998$ nm. Scherrer formula was used to calculate the size of the particles and the average crystallite size of the synthesized samples were found to be in the range 25–35 nm. SEM was used for surface morphology studies. SEM micrograph of the prepared samples showed small amount of agglomeration. Although PXRD showed that the prepared samples were pure, its purity was confirmed from the EDAX analysis. TEM results also confirmed that the particles are in nanosize. The optical band gap of the prepared samples is found to be higher than that of bulk Nd_2O_3. Upon 240 nm excitation, nanoparticles showed a series of emission bands in the UV and visible range. The optimal doping molar concentration was found to be 6% of samarium which gave the maximum intensity peak at 397 nm revealing that these materials are promising candidates in applications for solid state lightings specially near-ultraviolet light-emitting diodes (NUV-LEDs). The MEM/Rietveld analysis was done to determine the charge ordering behaviour with the inclusion of ions in the Nd_2O_3 matrix. The photoluminescent (PL) properties of the Nd_2O_3 and Sm^{3+} doped Nd_2O_3 nanophosphors were correlated with charge density properties.

Acknowledgements

One of the authors, Morris Marieli Antoinette, is grateful to the Management, The American College, Madurai for their continuous encouragement and support and also to Dr. G. Muralidharan, Department of Physics, Gandhigram Rural Institute, Dindigul, India for his great motivation and valuable discussions during this work.

References

1. Mortazavi-Derazkola S, Zinatloo-Ajabshir S, Salavati-Niasari M. Preparation and characterization of Nd_2O_3 nanostructures via a new facile solvent-less route. *J Mater Sci Mater Electron*. 2015;26:5658.
2. Pandurangappa C, Lakshminarasappa BN, Nagabhushana BM. Synthesis and characterization of CaF_2 nanocrystals. *J Alloys Compd*. 2010;489:592.
3. Tsuchiya T, Watanabe A, Nakajima T, Kumagai T. Preparation of Y_2O_3:Eu thin films by excimer-laser-assisted metal organic deposition. *Appl Phys A*. 2010;101:681.
4. He J, Pang Q, Li X, Liang CJ. Luminescence properties of YAG: Nd^{3+} nano-sized ceramic powders via co-microemulsion and microwave heating. *Bull Mater Sci*. 2013;36:1191.
5. Wang GF, Peng Q, Li YD. Lanthanide-doped nanocrystals: synthesis, optical-magnetic properties and applications. *Acc Chem Res*. 2011;44:322.
6. Zhang N, Yi R, Zhou LB, Gao GH, Shi RR, Qiu GZ, Liu XH. Lanthanide hydroxide nanorods and their thermal decomposition to lanthanide oxide nanorods. *Mater Chem Phys*. 2009;114:160.
7. Panda AB, Glaspell G, El-Shall MS. Microwave synthesis and optical properties of uniform nanorods and nanoplates of rare earth oxides. *J Phys Chem C*. 2007;111:1861.
8. Zhang ZJ, Shi J, Wang XY, Liu SD, Wang X. Vibrational and luminescent properties of $LaPO_4$:Eu^{3+} with different preparation conditions. *J Rare Earths*. 2016;34:1103.
9. Singh Jyoti, Baitha Pankaj Kumar, Manam J. Influence of heat treatment on the structural and optical properties of $SrGd_2O_4$:Eu^{3+} phosphor. *J Rare Earths*. 2015;33:1040.
10. Fu JP, Pang R, Jiang LH, Jia YL, Sun WZ, Zhang S, Li CY. A novel dichromic self-referencing optical probe SrO: Bi^{3+}, Eu^{3+} for temperature spatially and temporally imaging. *Dalton Trans*. 2016;45:13317.
11. Liu L, Jiang HL, Chen YJ, Zhang XL, Zhang ZG, Wang YX. Power dependence of upconversion luminescence of Er^{3+}doped Yttria nanocrystals and their bulk counterpart. *J Lumin*. 2013;143:423.
12. Fu JP, Zhang S, Pan R, Jia YL, Sun WZ, Li HF, Jiang LH, Li CY. Material and ingenious synthesis strategy for short-wavelength infrared light-emitting device. *Inorg Chem*. 2016;55:11258.
13. Umesh B, Eraiah B, Nagabhushana H, Sharma SC, Sunitha DV, Nagabhushana BM, Shivakumara C, Rao JL, Chakradhar RPS.

Thermoluminescence and EPR studies of nanocrystalline $Nd_2O_3:Ni^{2+}$ phosphor. *Spectrochim Acta Part A*. 2012;93:228.
14. Liu T, Zhang Y, Shao H, Li X. Synthesis and characteristics of Sm_2O_3 and Nd_2O_3 nanoparticles. *Langmuir*. 2003;19:7569.
15. Zawadzki M. Microwave-assisted synthesis and characterization of ultrafine neodymium oxide particles. *J Alloys Compd*. 2008;451:297.
16. Zawadzki M, Kepinski L. Synthesis and characterization of neodymium oxide nanoparticles. *J Alloys Compd*. 2004;380:255.
17. Liu G, Hong G, Wang J, Dong X. Hydrothermal synthesis of spherical and hollow $Gd_2O_3:Eu^{3+}$ phosphors. *J Alloys Compd*. 2007;432:200.
18. Fu Y, Wen S, Hsu C. Preparation and characterization of $Y_3Al_5O_{12}$: Ce and Y_2O_3: Eu phosphors powders by combustion process. *J Alloys Compd*. 2008;458:318.
19. Liu T, Meng QY, Sun WJ. Luminescent properties of Eu^{3+} doped $NaY(WO_4)_2$ nanophosphors prepared by molten salt method. *J Rare Earths*. 2015;33:915.
20. Chandrasekhar M, Nagabhushana H, Sudheerkumar KH, et al. Comparison of structural and luminescence properties of Dy_2O_3 nanopowders synthesized by co-precipitation and green combustion routes. *Mater Res Bull*. 2014;55:237.
21. Mendez M, Carvajal JJ, Cesteros Y, Aguilo M, Diaz F, Giguere A, Drouin D, Martinez-Ferrero E, Salagre P, Formentin P, Pallares J, Marsal LF. Sol–gel Pechini synthesis and optical spectroscopy of nanocrystalline La_2O_3 doped with Eu^{3+}. *Opt Mater*. 2010;32:1686.
22. Que W, Kam CH, Zhou Y, Lam YL, Chan YC. Yellow-to-violet upconversion in neodymium oxide nanocrystal/titania/ormosil composite sol–gel thin films derived at low temperature. *J Appl Phys*. 2001;90:4865.
23. Lupei V, Lupei A, Ikesue A. Transparent Nd and (Nd, Yb)-doped Sc_2O_3 ceramics as potential laser materials. *Appl Phys Lett*. 2005;86, 111118.
24. Shi DM, Zhao YG. Spectroscopic properties and energy transfer of Nd^{3+}/Ho^{3+}-doped Ga_2O_3-GeO_2 glass by codoping Yb^{3+} ion. *J Rare Earths*. 2016;34:368.
25. Ren JH, Zhao TG, Liu JH, Kong J, He JX, Guo L. Synthesis and photoluminescence properties of Nd_2O_3 nanoparticles modified by sodium bis(2-ethylhexyl) sulfosuccinate. *Chin Phys B*. 2008;17:4669.
26. Hodgson GK, Impellizzeri S, Hallett-Tapley GL, Scaiano JC. Photochemical synthesis and characterization of novel samarium oxide nanoparticles: toward a heterogeneous Bronsted acid catalyst. *RSC Adv*. 2015;5:3728.
27. El-Zaiat SY, El-Den MB, El-Kameesy SU, El-Gammam YA. Spectral dispersion of linear optical properties for Sm_2O_3 doped doped B_2O_3–PbO–Al_2O_3 glasses. *Opt Laser Technol*. 2012;44:1270.
28. Mandal B, Mondal A, Ray SS, Kundu A. Sm doped mesoporous CeO_2 nanocrystals: aqueous solution-based surfactant assisted low temperature synthesis, characterization and their improved autocatalytic activity. *Dalton Trans*. 2016;45:1679.
29. Lin H, Wang XY, Li CM, Li XJ, Tanabe S, Yu JY. Spectral power distribution and quantum yields of Sm^{3+}-doped heavy metal tellurite glass under the pumping of blue lighting emitting diode. *Spectrochim Acta Part A*. 2007;67:1417.
30. Zwayen A, Al-Juboori M. Rare earth (Sm^{3+} and Dy^{3+})-doped gadolinium oxide nanomaterials for luminescence thermometry. *Phys Scr*. 2013;T157:014004.
31. Annadurai G, Masilla Moses Kennedy S, Sivakumar V. Photoluminescence properties of a novel orange-red emitting $Ba_2CaZn_2Si_6O_{17}:Sm^{3+}$ phosphor. *J Rare Earths*. 2016;34:576.
32. Galceran M, Pujol MC, Aguilo M, Diaz F. Sol-gel modified Pechini method for obtaining nanocrystalline $KRE(WO_4)_2$ (RE=Gd and Yb). *J Sol Gel Sci Technol*. 2007;42:79.
33. William EB, Pujol MC, Cascales C, Carvajal JJ, Mateos X, Aguilo M, Diaz F. Synthesis and structural characterization of $Tm:Lu_2O_3$ nanocrystals. An approach towards new laser ceramics. *Opt Mater*. 2011;33:722.
34. Galceran M, Pujol MC, Carvajal JJ, Mateos X, Zaldo C, Aguilo M, Diaz F. Structural characterization and ytterbium spectroscopy in Sc_2O_3 nanocrystals. *J Lumin*. 2010;130:1437.
35. Galceran M, Pujol MC, Aguilo M, Diaz F. Synthesis and characterization of nanocrystalline $Yb:Lu_2O_3$ by modified Pechini method. *Mater Sci Eng B*. 2008;146:7.
36. Kulkarni SK. *"Analysis Techniques" in Nanotechnology: Principles and Practices*. New Delhi: Springer; 2015:169.
37. Willamson GK, Hall WH. X-ray line broadening from filed aluminum and wolfram. *Acta Metall*. 1953;1:22.
38. Carnall WT, Fields PR, Rajnak K. Electronic energy levels in the trivalent lanthanide aquo ions. I. Pr^{3+}, Nd^{3+}, Pm^{3+}, Sm^{3+}, Dy^{3+}, Ho^{3+}, Er^{3+}, and Tm^{3+}. *J Chem Phys*. 1968;49:4424.
39. Mortazavi-Derazkola S, Zinatloo-Ajabshir S, Salavati-Niasari M. *RSC Adv*. 2015;5:56666.
40. Lin H, Huang CP, Li W, Ni C, Ismat Shah S, Tseng Yao-Hsuan. Size dependency of nanocrystalline TiO_2 on its optical property and photocatalytic reactivity exemplified by 2-chlorophenol. *Appl Catal B*. 2006;68:1.
41. Umesh B, Eraiah B, Nagabhushana H, Nagabhushana BM, Nagaraja G, Shivakumara C, Chakradhar RPS. Synthesis and characterization of spherical and rod like nanocrystalline Nd_2O_3 phosphors. *J Alloys Compd*. 2011;509:1146.
42. Umesh B, Eraiah B, Nagabhushana H, Sharma SC, Nagabhushana BM, Shivakumara C, Rao JL, Chakradhar RPS. Structural, EPR, optical and Raman studies of $Nd_2O_3:Cu^{2+}$ nanophosphors. *Spectrochim Acta Part A*. 2012;94:365.
43. Rietveld HM. A profile refinement method for nuclear and magnetic structures. *J Appl Cryst*. 1969;2:65.
44. Petricek V, Dusek M, Paltinus L. Crystallographic computing system JANA2006: general features. *Z Krist*. 2014;229(5):345.
45. Eyring L. *Progress in the Science and Technology of the Rare Earths*. Oxford, England: Pergamon Press Ltd.; 1964.
46. Collins DM. Electron density images from imperfect data by iterative entropy maximization. *Nature*. 1982;298:49.
47. Syed Ali KS, Saravanan R, Israel S, Rajaram RK. Electron density distribution and bonding in ZnSe and PbSe using maximum entropy method (MEM). *Bull Mater Sci*. 2006;29:107.
48. Takata M. The MEM/Rietveld method with nano-applications – accurate charge-density studies of nano-structured materials by synchrotron-radiation powder diffraction. *Acta Cryst Sect A*. 2008;64:232.
49. Saravanakumar S, Sasikumar S, Israel S, Pradhiba GR, Saravanan R. Structural, magnetic and charge-related properties of nano-sized cerium manganese oxide, a dilute magnetic oxide semiconductor. *Mater Sci Semicond Process*. 2014;17:186.
50. Saravanakumar S, Saravanan R, Sasikumar S. Effect of sintering temperature on the magnetic properties and charge density distribution of nano- NiO. *Chem Pap*. 2014;68(6):788.
51. Saravanakumar S, Pattamimal M, Israel S, Sheeba RAJR, Saravanan R. The analysis on the rearrangement of charge density distribution in response to magnetic behavior in Mn doped SnO_2 nanoparticles. *Phys B*. 2012;407:302.
52. Ruben AD, Fujio I. *Super-fast Program PRIMA for the Maximum-Entropy Method*. vol. 305. 1-1 Namoki, Tsukuba, Ibaraki Japan: Advanced Materials Laboratory, National Institute for Materials Science; 2004:44.
53. Momma K, Izumi F. VESTA 3 for three-dimensional visualization of crystal, volumetric and morphology data. *J Appl Crystallogr*. 2011;44:1272.